



Article

Ag₃PO₄-Deposited TiO₂@Ti₃C₂ Petals for Highly Efficient Photodecomposition of Various Organic Dyes under Solar Light

Ngoc Tuyet Anh Nguyen and Hansang Kim *

Department of Mechanical Engineering, Gachon University, Seongnam 13120, Korea; anh2510@gachon.ac.kr
* Correspondence: hskim70@gachon.ac.kr; Tel.: +82-31-750-5307

Abstract: Two-dimensional Ti₃C₂ MXenes can be used to fabricate hierarchical TiO₂ nanostructures that are potential photocatalysts. In this study, the photodecomposition of organic dyes under solar light was investigated using flower-like TiO₂@Ti₃C₂, deposited using narrow bandgap Ag₃PO₄. The surface morphology, crystalline structure, surface states, and optical bandgap properties were determined using scanning electron microscopy (SEM), transmission electron microscopy (TEM), X-ray diffraction (XRD), X-ray photoelectron spectroscopy (XPS), nitrogen adsorption analysis, and UV-Vis diffuse reflectance spectroscopy (UV-DRS). Overall, Ag₃PO₄-deposited TiO₂@Ti₃C₂, referred to as Ag₃PO₄/TiO₂@Ti₃C₂, demonstrated the best photocatalytic performance among the as-prepared samples, including TiO₂@Ti₃C₂, pristine Ag₃PO₄, and Ag₃PO₄/TiO₂ P25. Organic dyes, such as rhodamine B (RhB), methylene blue (MB), crystal violet (CV), and methylene orange (MO), were efficiently degraded by Ag₃PO₄/TiO₂@Ti₃C₂. The significant enhancement of photocatalysis by solar light irradiation was attributed to the efficient deposition of Ag₃PO₄ nanoparticles on flower-like TiO₂@Ti₃C₂ with the efficient separation of photogenerated e⁻/h⁺ pairs, high surface area, and extended visible-light absorption. Additionally, the small size of Ag₃PO₄ deposition (ca. 4–10 nm diameter) reduces the distance between the core and the surface of the composite, which inhibits the recombination of photogenerated charge carriers. Free radical trapping tests were performed, and a photocatalytic mechanism was proposed to explain the synergistic photocatalysis of Ag₃PO₄/TiO₂@Ti₃C₂ under solar light.

Keywords: Ti₃C₂ MXene; Ag₃PO₄; photocatalyst; organic dyes; solar light; Ag₃PO₄/TiO₂@Ti₃C₂



Citation: Nguyen, N.T.A.; Kim, H. Ag₃PO₄-Deposited TiO₂@Ti₃C₂ Petals for Highly Efficient Photodecomposition of Various Organic Dyes under Solar Light. *Nanomaterials* **2022**, *12*, 2464. <https://doi.org/10.3390/nano12142464>

Academic Editors: Junying Zhang, Yong Chen and Jungang Hou

Received: 1 June 2022

Accepted: 9 July 2022

Published: 18 July 2022

Publisher's Note: MDPI stays neutral with regard to jurisdictional claims in published maps and institutional affiliations.



Copyright: © 2022 by the authors. Licensee MDPI, Basel, Switzerland. This article is an open access article distributed under the terms and conditions of the Creative Commons Attribution (CC BY) license (<https://creativecommons.org/licenses/by/4.0/>).

1. Introduction

Globally, as industrialization and urbanization accelerate, the demand for food and consumer goods (clothing, electronics, furniture, vehicles, etc.) increases. Unsustainable resource use and inefficient waste management, however, contribute to environmental problems, which have become a source of concern [1–3]. Numerous harmful pollutants endanger the environment and human health, such as heavy metal ions, toxic gases, and organic dye [4,5]. The majority of organic dyes found in wastewater originate from various industrial waste streams, including paint, dyeing clothing, bleaching paper, synthesizing rubber, and processing plastic, thereby, resulting in water pollution.

Organic dyes at high concentrations (5–1500 mg/L) cause significant environmental and organismal toxicity, including carcinogenic, mutagenic, and teratogenic effects [6–8]. Owing to their low removal capacity, conventional biological processes used to remove dyes, such as flocculation, filtration, precipitation, and coagulation, have gradually become obsolete [9,10]. In comparison, heterogeneous photocatalysts used in advanced oxidation processes are considered promising alternatives for the removal of a wide variety of organic pollutants with a highly efficient degradation rate [11].

Titania (TiO₂) is the most widely used and recognized photocatalytic material in environmental remediation owing to its superior photocatalytic performance, non-toxicity, and stability [12–14]. However, pure TiO₂ has a low quantum efficiency and a large

bandgap, limiting its application (i.e., electrons can be triggered only under UV light). In addition, the rapid recombination of photogenerated electron–hole pairs reduces its degradation efficiency [15]. Recently, several strategies have been proposed to solve these problems by fabricating TiO_2 derived from Ti_3C_2 [16].

Despite the absence of noble metal deposition (Au, Ag, Pt, Ru_2O , etc.), the flower-shaped $\text{TiO}_2@/\text{Ti}_3\text{C}_2$ composite exhibits significantly enhanced photocatalytic activity [4,17]. Recent work has been published on the synthesis of $\text{TiO}_2@/\text{Ti}_3\text{C}_2$ nanoflowers from the MAX phase (Ti_3AlC_2) [4,16,17]. They demonstrated that the presence of Ti_3C_2 in the TiO_2 structure eliminates electron–hole pair recombination, maximizes charging transfer, and expands the light absorption area to use visible light. Under solar light irradiation, the degradation efficiencies of RhB were 97% within 40 min and 95% within 60 min. Therefore, flower-shaped $\text{TiO}_2@/\text{Ti}_3\text{C}_2$ is a highly promising photocatalyst [4,16,17].

Silver-based semiconductor photocatalysts have been widely used due to their high efficiency as visible-light-driven photocatalysts [18]. Among silver-based photocatalysts, trisilver phosphate (Ag_3PO_4) with a narrow bandgap (2.36 eV) has attracted the photocatalytic field's attention due to its high oxidation capacity and ability to remove pollutants under visible light illumination [18–21]. Nevertheless, Ag_3PO_4 continues to fall short of meeting the demand for large-scale industrial applications, primarily due to its low reuse rates, as it suffers greatly from severe photocorrosion [22,23].

This is due to the intrinsic fast charge recombination, self-corrosion, and photocorrosion of silver or silver oxides in the absence of a sacrificial reagent. Therefore, the key strategy is to prevent its photocorrosion in practical applications. In this regard, heterostructure photocatalysts composed of Ag_3PO_4 and TiO_2 semiconductors have attracted attention over the years due to their increased photocatalytic efficiency, increased stability, and lower noble metal consumption [20]. To our knowledge, no research on the combination of Ag_3PO_4 and Ti_3C_2 -derived TiO_2 has been conducted.

Herein, an Ag_3PO_4 -deposited $\text{TiO}_2@/\text{Ti}_3\text{C}_2$ composite, $\text{Ag}_3\text{PO}_4/\text{TiO}_2@/\text{Ti}_3\text{C}_2$, was developed as a highly efficient visible photocatalyst. Flower-like TiO_2 was initially synthesized from Ti_3C_2 MXenes through three consecutive steps of hydrothermal oxidation, ion exchange, and heating processes [4,16,17]. Thereafter, using an in-situ precipitation method, Ag_3PO_4 nanoparticles (NPs) were deposited on flower-like $\text{TiO}_2@/\text{Ti}_3\text{C}_2$. It is conceivable that the presence of metal-like Ti_3C_2 in the $\text{TiO}_2@/\text{Ti}_3\text{C}_2$ composite acts as an “electron sink”, facilitating the highly efficient photodegradation of organic dyes.

In addition, the flower-like morphology has a high surface area and an efficient deposition of Ag_3PO_4 on $\text{TiO}_2@/\text{Ti}_3\text{C}_2$ petals, which effectively separates electron–hole pairs and improves the solar light harvesting capability. Ag_3PO_4 -deposited $\text{TiO}_2@/\text{Ti}_3\text{C}_2$ exhibited significant photocatalytic performance in the photodecomposition of a variety of organic dyes (including RhB, MB, CV, and MO).

2. Materials and Methods

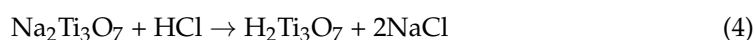
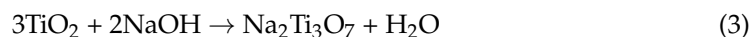
2.1. Chemical and Materials

Titanium carbide powder (Ti_3C_2 MXenes) was provided by Invisible Co. Ltd., Seoul, Korea. Sodium hydroxide (NaOH) was purchased from Daejung Chemicals & Metals Co., Ltd., Siheung, Korea. Silver nitrate (AgNO_3 , 99.9%) was obtained from Duksan Pure Chemicals Co., Ltd., Ansan, Korea. Hydrogen peroxide (H_2O_2 , 30%), hydrochloric acid (HCl), ethyl alcohol ($\text{C}_2\text{H}_5\text{OH}$), sodium phosphate (Na_3PO_4), methylene blue (MB), rhodamine B (RhB), methylene orange (MO), and crystal violet (CV) were purchased from Sigma-Aldrich, Munich, Germany. All chemicals were used directly, without any further treatment.

2.2. Preparation of $\text{TiO}_2@/\text{Ti}_3\text{C}_2$ Heterostructure

The procedure for fabricating flower-like $\text{TiO}_2@/\text{Ti}_3\text{C}_2$ was previously described by Vu Thi Quyen et al. [17]. First, 100 mg of Ti_3C_2 MXene was added and vigorously stirred for 15 min with a solution of 2 M NaOH (80 mL) and 30 wt% H_2O_2 (8 mL). Second, the hydrothermal reaction was performed by transferring the mixture into two 50 mL autoclave

systems at 140 °C for 15 h. The dispersion was then allowed to cool naturally to room temperature, and the samples were washed with deionized (DI) water and ethanol several times before being dried in an oven at 60 °C for 12 h. The dried sample was soaked in a 0.05 M HCl solution (500 mL) for 12 h to ensure ion exchange. After heating the sample in a furnace at 500 °C for 5 h, the TiO₂@Ti₃C₂ composite was obtained. The formation of TiO₂ is presented by the following equations:



2.3. Preparation of Ag₃PO₄ Particles

To prepare Ag₃PO₄ particles, a simple method was followed. To generate Ag₃PO₄, 0.1 M Na₃PO₄ (8 mL) was added dropwise to 0.1 M AgNO₃ solution (24 mL) and stirred for 5 h in the dark. To remove redundant ions, the precipitate was centrifuged and washed with deionized water. The purified sample was dried overnight at 60 °C to obtain the Ag₃PO₄ powder.

2.4. Preparation of Ag₃PO₄/TiO₂@Ti₃C₂

Ag₃PO₄/TiO₂@Ti₃C₂ composites were prepared by adding various amounts of AgNO₃ (x) and Na₃PO₄ (y) solutions with a ratio of x:y = 3:1. First, 0.05 g TiO₂@Ti₃C₂ was added to 0.1 M AgNO₃ solutions. The mixed solutions were vigorously stirred and sonicated for 10 min. Thereafter, 0.1 M Na₃PO₄ was gradually dropped into the solution and stirred for 5 h to form Ag₃PO₄. To avoid photocorrosion, the reaction was conducted in the dark. The resulting powder products were washed, centrifuged with DI water, and dried at 60 °C to obtain Ag₃PO₄/TiO₂@Ti₃C₂. The powder obtained from mixing quantities x = 1, 2, 4, 6, and 8 mL AgNO₃ with y = 0.33, 0.67, 1.33, 2, and 2.67 mL Na₃PO₄ corresponds to samples marked A1 to A5, respectively). The samples were kept in the dark throughout the preparation process to avoid photocorrosion. In comparison with sample A4, Ag₃PO₄/TiO₂ P25 was also prepared under the same conditions.

The fabrication procedure for the composites is depicted in Scheme 1. First, Ti₃C₂ MXene was subjected to hydrothermal oxidation, ion exchange, and heat treatment steps, transforming its accordion-like structure into a flower shape. Thereafter, Ag₃PO₄ NPs containing varying amounts of Ag₃PO₄ were deposited by in-situ precipitation on the flower-like structure to form the Ag₃PO₄/TiO₂@Ti₃C₂ composites. Photodegradation tests were conducted under solar-driven light.

2.5. Photocatalysis of Dye Degradation

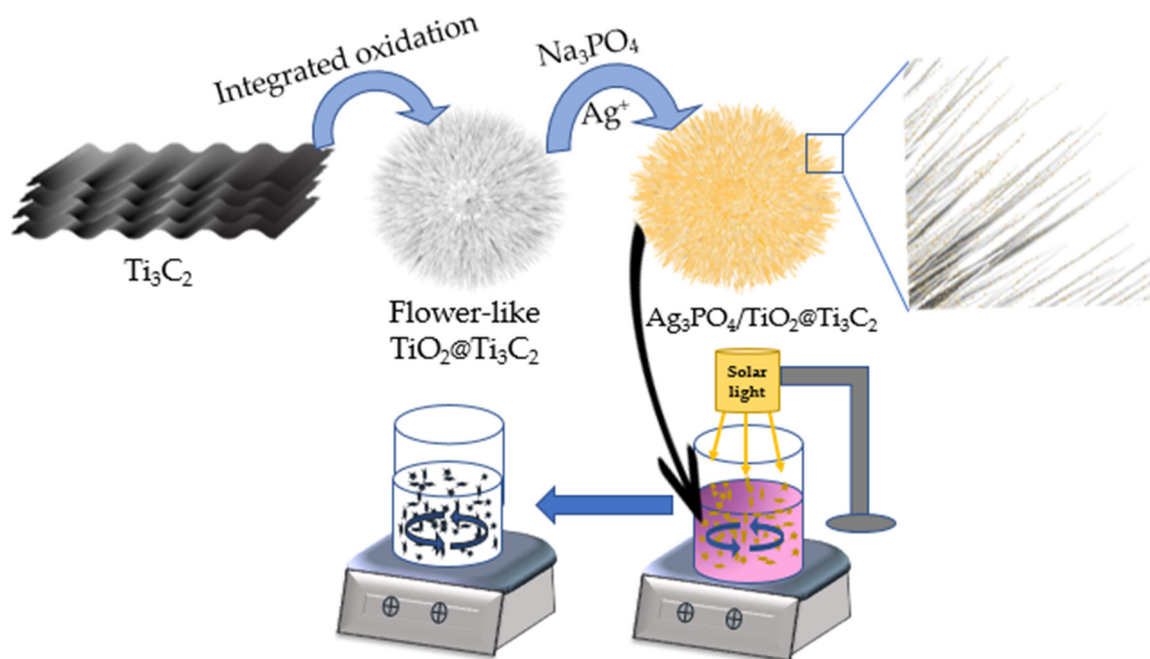
A Xe lamp (1000 W) was used as an artificial solar light source with a light intensity of 1000 mW/cm². Under simulated solar light, the photocatalytic activities of the as-prepared samples were evaluated for the photodecomposition of RhB dye. Typically, 10 mg of each sample was added to 20 mL of an aqueous solution containing RhB (9 mg/L). Prior to light irradiation, the adsorption experiments of Ag₃PO₄, TiO₂, and Ag₃PO₄/TiO₂@Ti₃C₂ were performed by stirring the solutions in the dark for 15 min to improve dispersion and adsorption–desorption equilibrium. Thereafter, the solution was exposed to solar light. Following that, an aliquot of each sample (1 mL) was removed and centrifuged at the indicated intervals to obtain the supernatant for UV-vis spectrophotometer evaluation.

The degradation efficiency of the dye materials can be described by the following equation: degradation percentage (%) = $C_0 - C_t / C_0 \times 100$. To determine the rate constant

of RhB degradation, the degradation kinetics were assumed to follow the pseudo-first order model [21,24]:

$$-\ln \frac{C}{C_0} = kt$$

where C_0 and C_t denote the initial concentration of RhB and a specific concentration of RhB after exposure to light for t minutes, respectively. Here, “ k ” is the pseudo-first-order rate constant calculated from the linear slope of $\ln(C_0/C)$ versus t (time). 10 mg/L concentration of MB, MO, and CV were used for photodegradation with the same procedure. The absorbance changes for each dye were determined using a UV-Vis spectrometer at different wavelengths, RhB (554 nm), MB (664–665 nm), MO (464 nm), and CV (590 nm).



Scheme 1. Schematic indicating the fabrication processes, beginning with multilayer Ti_3C_2 MXene and ending with the formation of Ag_3PO_4 -deposited flower-shaped $\text{TiO}_2@ \text{Ti}_3\text{C}_2$.

2.6. Characterization

The X-ray diffraction (XRD) patterns of the samples were determined using a Rigaku Smartlab X-ray diffractometer with $\text{Cu-K}\alpha$ radiation ($\lambda = 1.544 \text{ \AA}$) (Rigaku Corporation, Tokyo, Japan). The morphologies and microstructures of the samples were investigated using a Hitachi S-4700 field emission scanning electron microscope (FE-SEM) (Hitachi Ltd., Tokyo, Japan) and FEI Tecnai transmission electron microscopy (TEM) (FEI, Hillsboro, OR, United States). XPS measurements were conducted using an X-ray photoelectron spectrometer (XPS, Multilab 2000, Thermo Scientific, Waltham, MA, United States). The surface area, pore size, and pore volume were measured using an N_2 adsorption–desorption apparatus (ASAP 2020, Micromeritics Instrument Corp, Norcross, GA, USA). Optical properties of the samples were determined using a Jasco V770 UV-Vis diffuse reflectance spectrophotometer (Jasco Inc., Easton, MD, USA).

3. Results and Discussion

3.1. XRD Analysis

The diffraction patterns of the $\text{TiO}_2@ \text{Ti}_3\text{C}_2$, Ag_3PO_4 , and A4 samples are shown in Figure 1a. The XRD data of Ag_3PO_4 revealed sharp and narrow dominant peaks at 33.3° (210) and 36.6° (211), which corresponded to the body-centered crystal structure and high crystallinity (JCPDS no. 06-0505) [25]. Furthermore, $\text{TiO}_2@ \text{Ti}_3\text{C}_2$ exhibited a distinct peak at $2\theta = 25.3^\circ$, indicating the high crystallinity of the anatase phase with other weaker peaks

at 37.8° , 53.9° , 55.34° , and 62.6° (JCPDS card No. 21-1272) [21]. A small peak at 48.5° confirmed the presence of Ti_3C_2 in the sample [4,16,17].

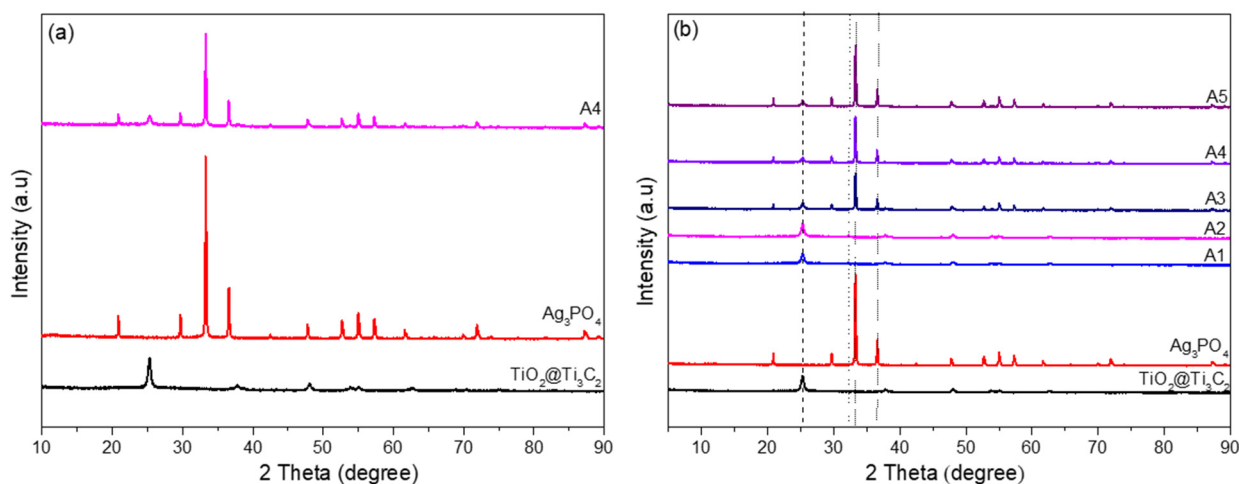


Figure 1. XRD patterns of as-prepared samples: (a) $\text{TiO}_2@/\text{Ti}_3\text{C}_2$, Ag_3PO_4 , and optimized A4 sample. (b) Additional XRD patterns of A1, A2, A3, and A5 samples, including A4.

In the case of the composites, Figure 1b shows the diffraction patterns of $\text{Ag}_3\text{PO}_4/\text{TiO}_2@/\text{Ti}_3\text{C}_2$ (samples A3, A4, and A5), which clearly display both Ag_3PO_4 crystal and TiO_2 anatase phase peaks, confirming that the composites were composed of Ag_3PO_4 and TiO_2 . The diffraction peaks of TiO_2 in the heterostructure composite are weaker than those of Ag_3PO_4 owing to the lower crystallinity of TiO_2 . However, samples A1 and A2 containing a lower concentration of Ag_3PO_4 mostly exhibit peaks of TiO_2 anatase at $= 25.3^\circ$ (JCPDS card No. 21-1272), instead of Ag_3PO_4 peaks due to self-corrosion [22].

3.2. Morphology Analysis by SEM, TEM

The accordion-like shape of Ti_3C_2 is shown in the SEM image in Figure 2a. After oxidization, ion exchange, and heat treatment, accordion-shape Ti_3C_2 transforms into $\text{TiO}_2@/\text{Ti}_3\text{C}_2$ with a flower shape (Figure 2b). Figure 2c depicts pure Ag_3PO_4 NPs with an irregular shape and a diameter of ca. 300–500 nm [19]. The SEM image in Figure 2d shows aggregated Ag_3PO_4 -deposited $\text{TiO}_2@/\text{Ti}_3\text{C}_2$ that retains its flower-like shape. To overcome certain limitations of SEM analysis, which focuses on the surface morphology of samples, TEM and HRTEM images were used to clarify the transmission morphology and crystalline structure of $\text{Ag}_3\text{PO}_4/\text{TiO}_2@/\text{Ti}_3\text{C}_2$ (sample A4). According to the EDX spectrum (Figure S1), the main elements present in the sample are carbon, oxygen, titanium, silver, and phosphorous. C, O, and Ti were obtained from $\text{TiO}_2@/\text{Ti}_3\text{C}_2$, with a portion of the O derived from Ag_3PO_4 . It can be demonstrated that Ag_3PO_4 is coated on the surface of $\text{TiO}_2@/\text{Ti}_3\text{C}_2$.

Figure 3a shows a typical TEM image of the flower-shaped $\text{TiO}_2@/\text{Ti}_3\text{C}_2$ with some petal fragments and large agglomerated Ag_3PO_4 on it. However, the higher magnification images in Figure 3b,c demonstrate that the dominant Ag_3PO_4 NPs were formed and deposited on each $\text{TiO}_2@/\text{Ti}_3\text{C}_2$ nanorod. Positively charged silver ions were attracted to the surface of negatively charged TiO_2 , and the reaction between Ag^+ and PO_4^{3-} occurred immediately upon the addition of Na_3PO_4 solution, resulting in the deposition of Ag_3PO_4 NPs on $\text{TiO}_2@/\text{Ti}_3\text{C}_2$ rods [26]. The TEM images show that precipitating Ag_3PO_4 using $\text{TiO}_2@/\text{Ti}_3\text{C}_2$ nanorods as a template can reduce particle aggregation owing to the high specific surface area of the nanorods, which affects Ag_3PO_4 nucleation and reduces the diameter to around 4–10 nm.

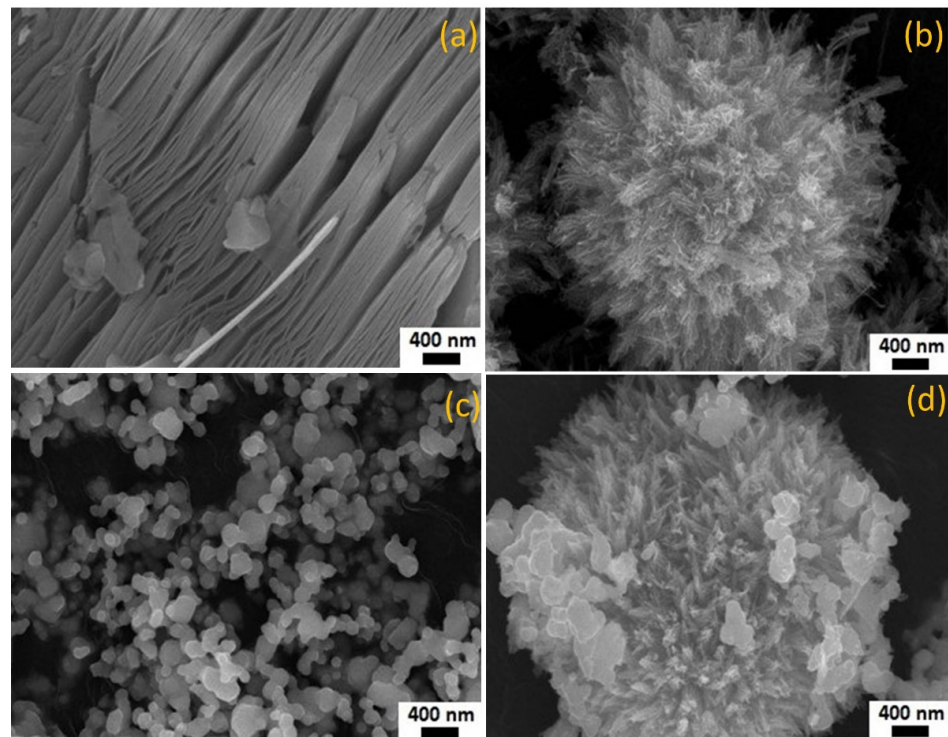


Figure 2. SEM images of (a) Ti₃C₂, (b) TiO₂@Ti₃C₂, (c) Ag₃PO₄, and (d) Ag₃PO₄/TiO₂@Ti₃C₂ (A4) samples.

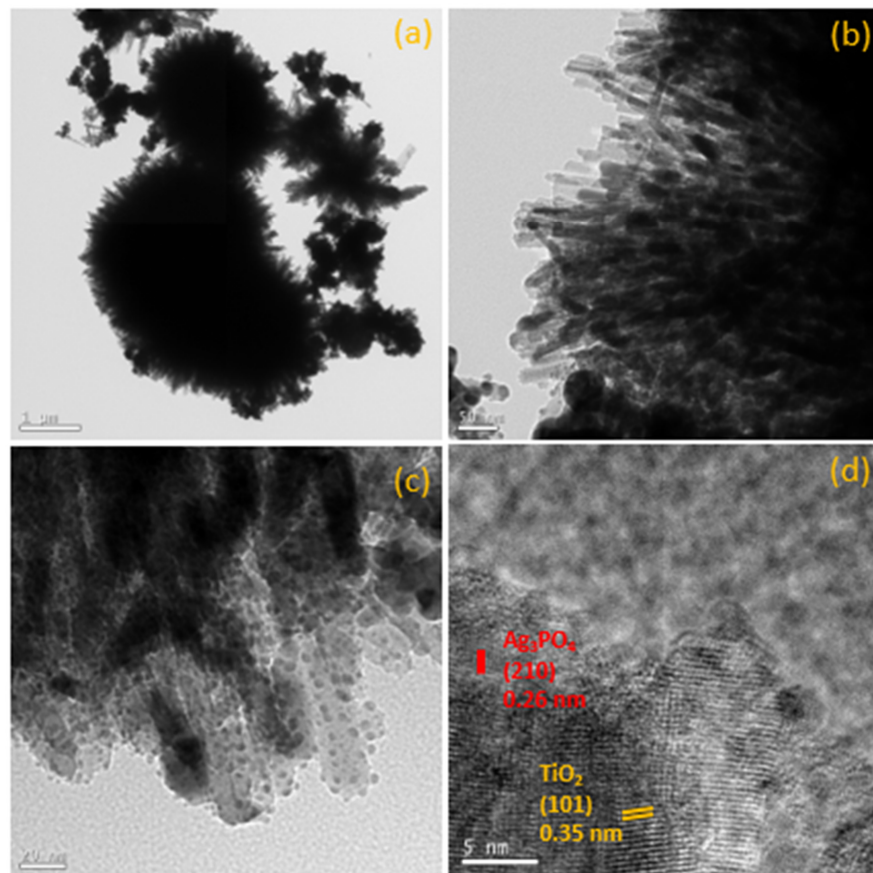


Figure 3. (a–c) TEM images of Ag₃PO₄/TiO₂@Ti₃C₂ (sample A4) viewed under different magnifications. (d) HR-TEM lattice image of Ag₃PO₄/TiO₂@Ti₃C₂.

Additionally, the Ag_3PO_4 nanoparticles were relatively stable and did not detach during sonication as part of the TEM preparation process, whereas the agglomerated Ag_3PO_4 fragments moved and changed position during real-time TEM measurements. Figure 3c,d show the high-resolution TEM (HR-TEM) images of the $\text{Ag}_3\text{PO}_4/\text{TiO}_2@\text{Ti}_3\text{C}_2$ composite. $\text{TiO}_2@\text{Ti}_3\text{C}_2$ (101) has lattice fringes with an interplanar spacing of 0.35 nm, while cubic Ag_3PO_4 (210) has an interplanar spacing of 0.26 nm (Figure 3d). A SAED image further demonstrates the clear formation and polycrystallinity of these materials, which is shown in Figure S2. These TEM images can assist in resolving the initial ambiguity regarding the morphology of $\text{Ag}_3\text{PO}_4/\text{TiO}_2@\text{Ti}_3\text{C}_2$ shown in the SEM images.

Figure 4 depicts the scanning TEM (STEM) image of $\text{Ag}_3\text{PO}_4/\text{TiO}_2@\text{Ti}_3\text{C}_2$ with elemental mapping. The high-angle annular dark-field (HAADF) STEM image of $\text{Ag}_3\text{PO}_4/\text{TiO}_2@\text{Ti}_3\text{C}_2$ shows areas with different contrasts, with the brighter regions representing Ag_3PO_4 particles and the darker regions representing $\text{TiO}_2@\text{Ti}_3\text{C}_2$ rods. The elemental mapping analysis displays C, O, P, K, and Ag elements from an arbitrary area. In detail, the Ti signal is primarily associated with the backbone of $\text{TiO}_2@\text{Ti}_3\text{C}_2$, whereas the P and Ag signals are associated with the large agglomerated Ag_3PO_4 fragments on top of the flower and Ag_3PO_4 NPs decorated alongside the petals. Additionally, the O signals are distributed uniformly throughout the composite. The elemental mapping results provide more comprehensive and clear observations of the elemental distribution across the whole composite, corresponding to the SEM and HR-TEM above.

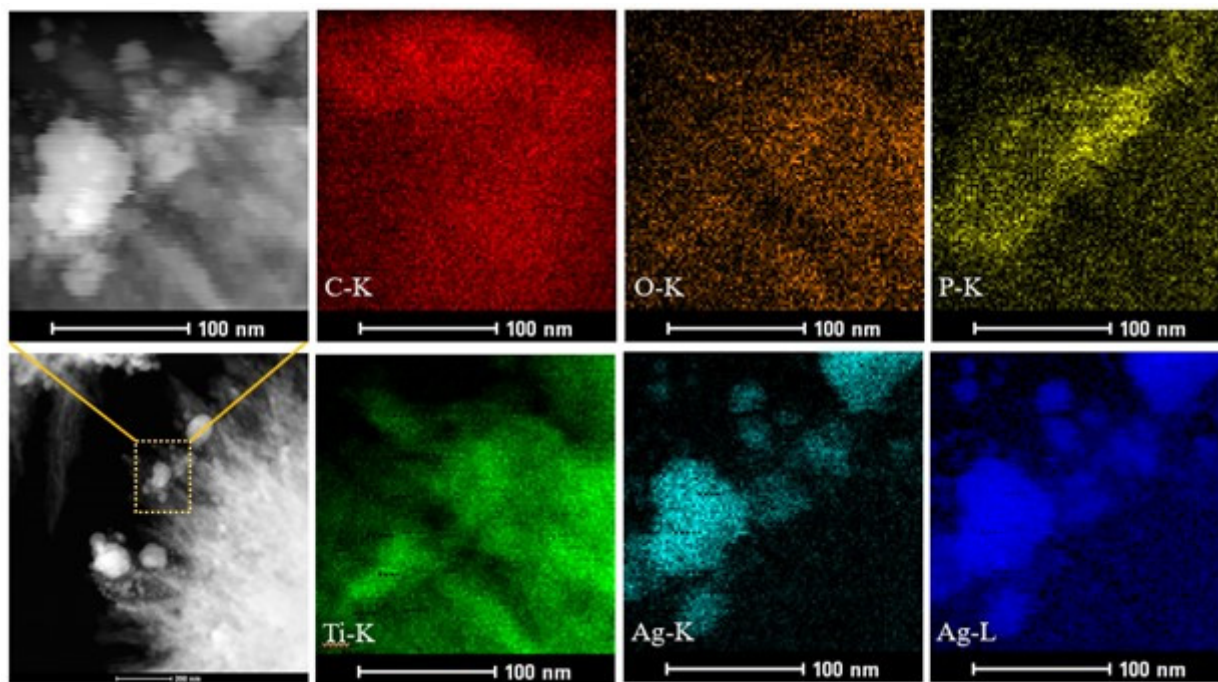


Figure 4. STEM images of $\text{Ag}_3\text{PO}_4/\text{TiO}_2@\text{Ti}_3\text{C}_2$ (sample A4) with element mapping (C, O, P, Ti, and Ag).

3.3. XPS Results

To characterize the chemical compositions and elemental states of the as-prepared samples, XPS measurements were conducted. The survey spectra of Ti_3C_2 MXene, $\text{TiO}_2@\text{Ti}_3\text{C}_2$ flowers, and $\text{Ag}_3\text{PO}_4/\text{TiO}_2@\text{Ti}_3\text{C}_2$ illustrate the characteristic elemental peaks at approximately 532.35, 455.16, and 284.96 eV allocated to O 1s, Ti 2p, and C 1s, respectively (Figure S3). The weak peak of F 1s at 685.1 eV in Ti_3C_2 , indicates that some fluoride was left over from the synthesis process [17].

The $\text{TiO}_2@\text{Ti}_3\text{C}_2$ heterostructure exhibits a much stronger O 1s peak intensity when compared to Ti_3C_2 , indicating the existence of an appreciable amount of oxide in the heterostructure due to the oxidation process and the formation of TiO_2 [4]. In the spectra

results of composite $\text{Ag}_3\text{PO}_4/\text{TiO}_2@\text{Ti}_3\text{C}_2$, the peaks of P 2p and Ag 3d represent Ag_3PO_4 in the composite. Generally, Ag 3d peaks have a higher intensity than Ti 2p, suggesting that many silver elements or their compounds are present on the surface of the solid sample, decorating the $\text{TiO}_2@\text{Ti}_3\text{C}_2$ flower shape. This result is consistent with the SEM and TEM images discussed previously.

Figure 5 demonstrates the Ti 2p, C 1s, and O 1s high-resolution spectra of Ti_3C_2 , $\text{TiO}_2@\text{Ti}_3\text{C}_2$, and $\text{Ag}_3\text{PO}_4/\text{TiO}_2@\text{Ti}_3\text{C}_2$ (sample A4). The Ti-C peak at 454.26 eV in Ti 2p spectra indicates the presence of Ti_3C_2 ; however, there is no Ti-C peak in $\text{TiO}_2@\text{Ti}_3\text{C}_2$ [27,28]. Additionally, the intensification of the Ti-O peak (Ti^{4+}) at 458.83 eV indicates the formation of TiO_2 in the flower-shaped $\text{TiO}_2@\text{Ti}_3\text{C}_2$. The Ti-C bond is absent in $\text{TiO}_2@\text{Ti}_3\text{C}_2$ in the high-resolution C 1s; however, C-C/C-H, C-O, and O-C = O bonds exist at approximately 284.88, 286.40, and 288.72 eV, respectively [28–30]. Owing to the use of $\text{TiO}_2@\text{Ti}_3\text{C}_2$ as a template for precipitate Ag_3PO_4 , the Ti 2p and C 1s spectra of $\text{Ag}_3\text{PO}_4/\text{TiO}_2@\text{Ti}_3\text{C}_2$ (sample A4) are similar to those of $\text{TiO}_2@\text{Ti}_3\text{C}_2$.

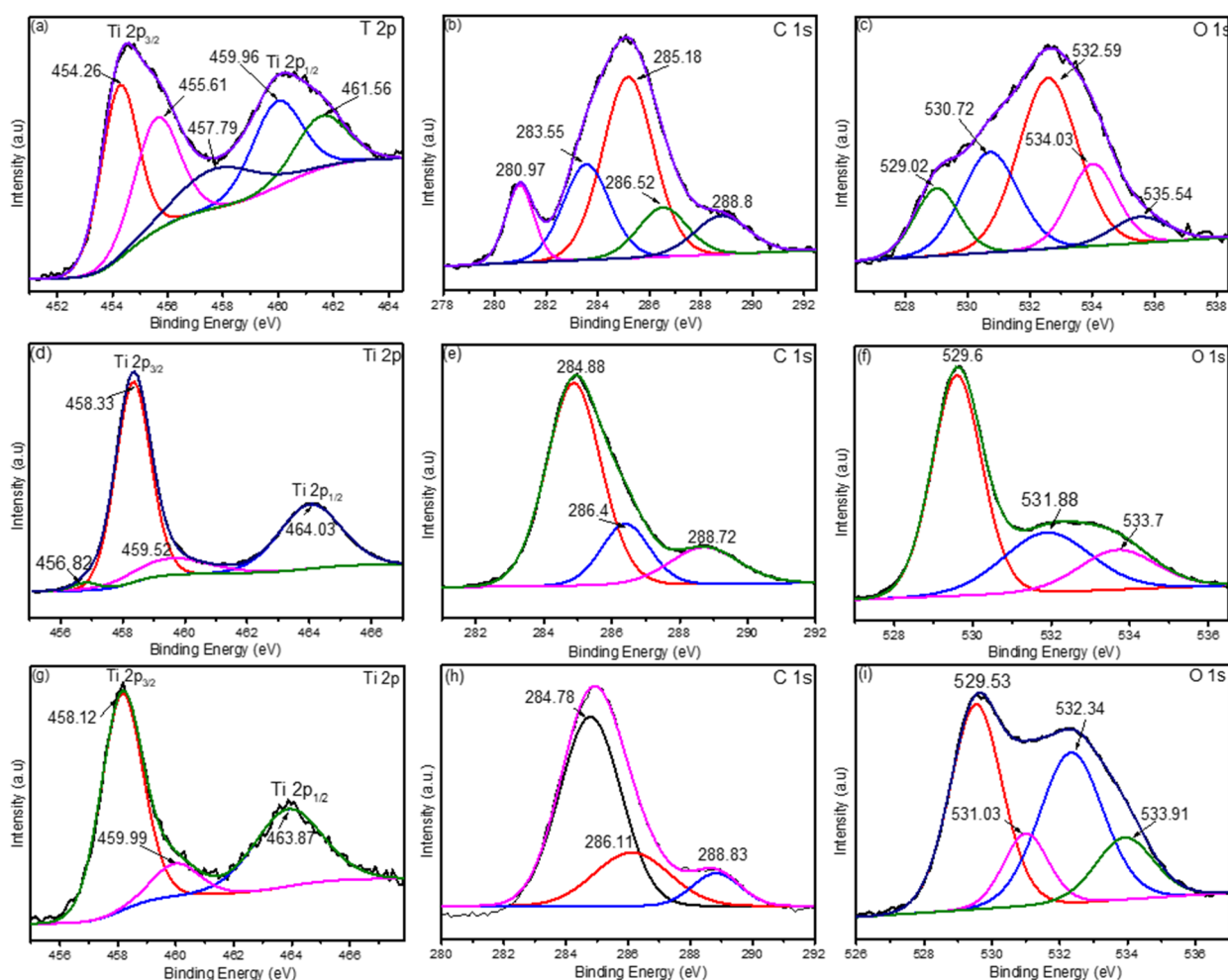


Figure 5. Ti 2p, C 1s, and O 1s high-resolution XPS spectra of Ti_3C_2 (a–c), $\text{TiO}_2@\text{Ti}_3\text{C}_2$ (d–f), and $\text{Ag}_3\text{PO}_4/\text{TiO}_2@\text{Ti}_3\text{C}_2$ (A4) (g–i).

Nevertheless, the differences in O 1s XPS spectra among the three samples were unavoidable owing to the changing environment in which oxygen was present. Ti_3C_2 exhibited a distinct peak attributed to C-Ti-OH linkage at 530.72 and 532.59 eV, whereas the others showed the strongest Ti-O peak at 529.60 eV. Furthermore, Ti_3C_2 MXene also exhibited F 1s spectra (Figure S4a), which could be ascribed to residual fluorine after the etching steps. The Ag 3d and P 1s spectra of $\text{Ag}_3\text{PO}_4/\text{TiO}_2@\text{Ti}_3\text{C}_2$ (sample A4) are presented in Figure S4b,c.

The binding energies of 366.83 and 372.91 eV assigned to Ag 3d_{5/2} and Ag 3d_{3/2}, respectively, indicate that Ag⁺ is dominated in the composites. The deconvoluted Ag 3d peaks are slightly shifted toward lower binding energy, and the FHMW is also wider. This is attributed to self-corrosion after exposure to the environment for a period of time [22]. The peak of the P 2p spectra located at 131.82 eV corresponds to P⁵⁺ in the PO₄³⁺ [31].

3.4. Surface Area and Optical Analysis

The N₂ adsorption–desorption isotherms and the corresponding BET surface areas, pore volumes, and pore sizes of TiO₂@Ti₃C₂, Ag₃PO₄/P25, and Ag₃PO₄/TiO₂@Ti₃C₂ are shown in Figure 6a and Table 1. Based on the isotherm curves, all samples belong to type IV, and the pore size indicates that they are mesopores [4]. As can be seen, the TiO₂@Ti₃C₂ flowers have the highest BET surface area (53 m²g^{−1}). After the deposition of Ag₃PO₄, the surface area and pore volume of the Ag₃PO₄/TiO₂@Ti₃C₂ sample (40 m²g^{−1}) decreased slightly but remained higher than that of Ag₃PO₄/TiO₂ P25 (27 m²g^{−1}). This high surface area enables photocatalytic reactions to occur.

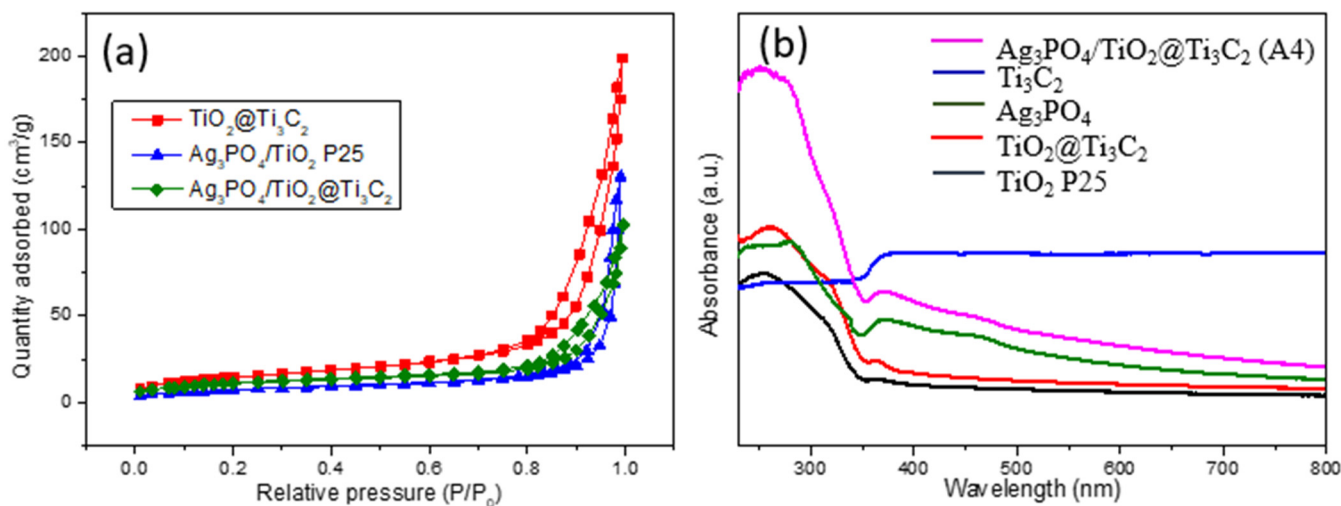


Figure 6. (a) BET surface area plot of TiO₂@Ti₃C₂, Ag₃PO₄/P25, and Ag₃PO₄/TiO₂@Ti₃C₂; (b) UV-Vis DRS spectra of the as-prepared samples, including pristine TiO₂ P25, TiO₂@Ti₃C₂, pure Ag₃PO₄, and Ag₃PO₄/TiO₂@Ti₃C₂ (sample A4).

Table 1. Specific surface area, pore volume, and pore size distribution of TiO₂@Ti₃C₂, Ag₃PO₄/TiO₂ P25, and Ag₃PO₄/TiO₂@Ti₃C₂ (sample A4).

Sample	BET Surface Area (m ² g ^{−1})	Pore Volume (cm ³ g ^{−1})	Pore Size (nm)
TiO ₂ @Ti ₃ C ₂	53	0.309	21.91
Ag ₃ PO ₄ /TiO ₂ P25	27	0.202	31.04
Ag ₃ PO ₄ /TiO ₂ @Ti ₃ C ₂ (A4)	40	0.156	20.12

The light-harvesting capability is important for evaluating photocatalytic activity as demonstrated by UV-Vis absorption spectra in Figure 6b. Owing to its metallic properties, Ti₃C₂ MXene exhibits a nearly horizontal spectrum over the entire wavelength range. The sequential transformations of MXene (metallic material) to the TiO₂@Ti₃C₂ heterostructure (semiconductor material) throughout the processes resulted in the gradual development of the TiO₂@Ti₃C₂ absorption peak [4,16,17]. Its light absorption is improved compared with that of the commercial TiO₂ P25.

It can be seen that the decoration of Ag₃PO₄ on the flower-shaped TiO₂@Ti₃C₂ extends the optical absorption by the combination of Ag₃PO₄ and TiO₂@Ti₃C₂. Due to the high surface area of the 3D nanoflower structure, the harvested and scattered light

is omnidirectional. In this case, the forward and backward light results in constructive interference, which can extend the photon lifetime and improve the absorbance [16]. These findings further confirm that the Ag_3PO_4 -deposited $\text{TiO}_2@/\text{Ti}_3\text{C}_2$ composite can enhance the light-harvesting ability, making it a promising photocatalyst under visible illumination.

3.5. Photocatalytic Performance

3.5.1. The Effects of Ag_3PO_4 Content on the Photodegradation of Rhodamine B

Figure 7a illustrates the photocatalytic degradation of RhB (9 mgL^{-1}) using Ag_3PO_4 , TiO_2 and $\text{Ag}_3\text{PO}_4/\text{TiO}_2@/\text{Ti}_3\text{C}_2$ composites (samples A1, A2, A3, A4, and A5) at a concentration of 0.5 gL^{-1} under solar light irradiation. Overall, the composite exhibited effective photodegradation reaction under solar light irradiation in a short period of time, with sample A4 displaying significant enhanced photocatalytic performance by demonstrating 97% RhB degradation within 12 min.

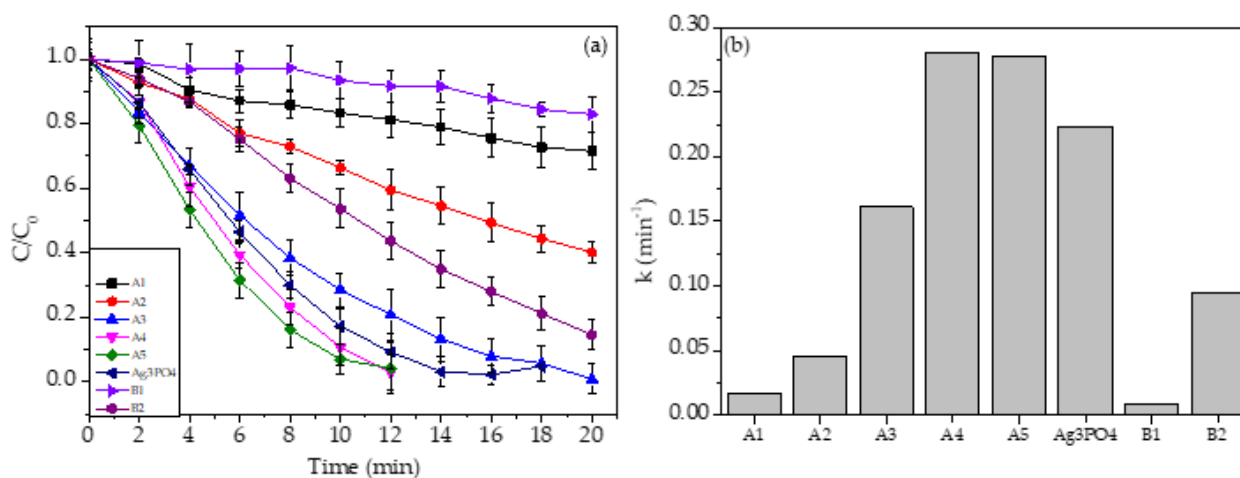


Figure 7. (a) Photocatalytic performance and (b) the rate constant of $\text{Ag}_3\text{PO}_4/\text{TiO}_2@/\text{Ti}_3\text{C}_2$ composite (samples A1, A2, A3, A4, and A5), pure Ag_3PO_4 , $\text{TiO}_2@/\text{Ti}_3\text{C}_2$ (B1), and $\text{Ag}_3\text{PO}_4/\text{TiO}_2$ P25 (B2).

As samples A1 and A2 contain less Ag_3PO_4 and may be susceptible to self-corrosion and photocorrosion, as discussed in the XRD diffractogram, these samples took 20 min to partially degrade 28.9% and 59.9% RhB, respectively. Although sample A5 contains more Ag_3PO_4 than sample A4, there was no significant difference in the photocatalytic activities between samples A5 and A4. When comparing degradation performances within 20 min, pure Ag_3PO_4 had a degradation efficiency of 95% and $\text{Ag}_3\text{PO}_4/\text{TiO}_2$ P25 86%. The lower photocatalytic performance of $\text{Ag}_3\text{PO}_4/\text{TiO}_2$ P25 is most likely due to self-corrosion in the composite after prolonged storage [22].

Figure 7b shows the calculated rate constant (k) values of 0.017, 0.046, 0.161, 0.289, and 0.278; 0.223; 0.095 min^{-1} ; and 0.0093 min^{-1} for samples A1–A5, Ag_3PO_4 , $\text{Ag}_3\text{PO}_4/\text{TiO}_2$ P25, and flower-like $\text{TiO}_2@/\text{Ti}_3\text{C}_2$, respectively. These results indicate that, among the as-prepared samples, sample A4 exhibited the greatest photocatalysis performance. These results indicate that combining TiO_2 derived from MXene with Ag_3PO_4 can significantly improve its photocatalytic performance when exposed to solar illumination.

3.5.2. Photodegradation of Other Organic Dyes

The three dyes, MB, CV, and MO (10 mg L^{-1} , 0.5 gL^{-1}) were also photodegraded under solar light irradiation. The adsorption and photocatalytic performance of sample A4 over time for the three organic dyes are shown in Figures 8b and S5. The results indicate that the composite is effective in adsorbing cationic dyes (MB and CV) but has no effect on anionic dye concentration (MO) after 15 min in the dark. It can be attributed to the composite's surface, which is anionic and negatively charged in the aqueous solution, which enables it to readily attract and adsorb cationic dyes in comparison to its anionic dye

counterpart [32]. These results aid in the cationic dyes' molecules more easily reaching the surface of materials, leading to higher degradation performance in MB and CV compared to MO. After 6 min, the photocatalyst degraded 94.4% of MB, nearly 99.2% CV in 14 min, and 92.4% MO after 40 min. The pseudo-first-order rate constants for MB, CV, and MO were calculated to be 0.489, 0.279, and 0.073 min^{-1} , respectively.

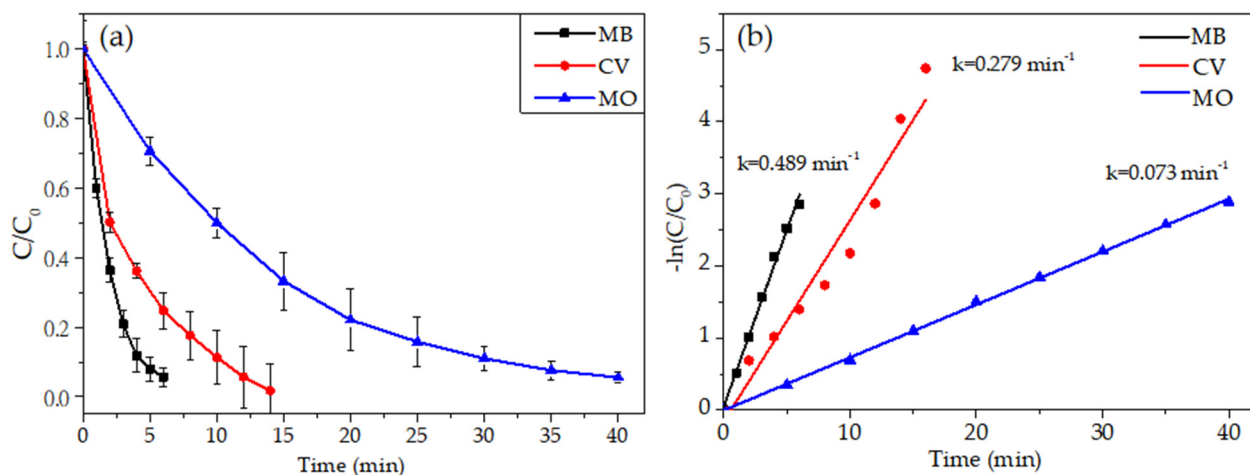


Figure 8. (a) Photocatalytic results of $\text{Ag}_3\text{PO}_4/\text{TiO}_2@\text{Ti}_3\text{C}_2$ (sample A4) and (b) the corresponding rate constants for organic dyes.

Compared with $\text{TiO}_2@\text{Ti}_3\text{C}_2$, pristine Ag_3PO_4 , and $\text{Ag}_3\text{PO}_4/\text{TiO}_2$ P25, the $\text{Ag}_3\text{PO}_4/\text{TiO}_2@\text{Ti}_3\text{C}_2$ composite exhibited superior photocatalytic activity. Recent publications on photocatalytic materials indicate the possibility of a highly promising photocatalyst for flower shaped $\text{TiO}_2@\text{Ti}_3\text{C}_2$ with a high surface area. Combining $\text{TiO}_2@\text{Ti}_3\text{C}_2$ with Ag_3PO_4 results in synergetic photodegradation of various dyes. The flower-like structure of TiO_2 derived from Ti_3C_2 can improve its light-harvesting ability, and its high specific surface area allows the solvent to approach the reactive sites more easily.

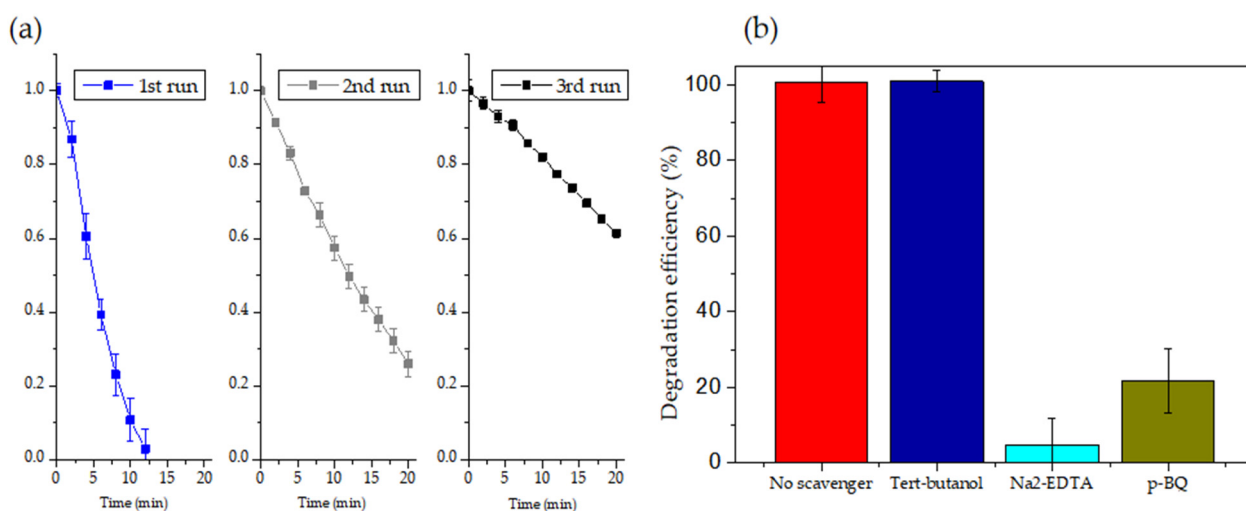
Additionally, Ag_3PO_4 in the composites can shorten the diffusion paths for photoexcited carriers, thereby, inhibiting the recombination of electron–hole pairs [4,25]. The photocatalytic activity of the optimized sample was compared to that of other reported similar photocatalysts. As demonstrated in Table 2, the $\text{Ag}_3\text{PO}_4/\text{TiO}_2@\text{Ti}_3\text{C}_2$ composite (sample A4) can degrade a variety of pollutants, including both cationic and anionic dyes, in a relatively short period of time, as compared to the state-of-the-art works listed in Table 2.

3.6. Scavenger Trapping and Recycling Tests of RhB Degradation

To ascertain the main active species in the photocatalytic reactions, scavenger trapping tests were conducted on RhB photodegradation over the $\text{Ag}_3\text{PO}_4/\text{TiO}_2@\text{Ti}_3\text{C}_2$ composite (sample A4). The three types of scavengers were tert-butanol (a quencher of $\bullet\text{OH}$), $\text{Na}_2\text{-EDTA}$ (a quencher of h^+), and p-benzoquinone (p-BQ, a quencher of $\bullet\text{O}_2^-$). The dye solution containing a specified amount of catalyst was added to 2 mL of trapping agent (0.01 M), stirred for 15 min in the dark, and exposed to solar light for 20 min. As shown in Figure 9a, the addition of tert-butanol had no effect on the photocatalytic performance, thereby, indicating that free $\bullet\text{OH}$ radicals were not the dominant oxidizing species. The presence of $\text{Na}_2\text{-EDTA}$ and p-BQ, however, decreased the degradation efficiency to 4.76% and 21.7%, respectively. From these results, it can be concluded that h^+ and $\bullet\text{O}_2^-$ radicals play a critical role in the photodecomposition of RhB.

Table 2. A comparison of the photocatalytic efficiency of TiO₂@Ti₃C₂ and Ag₃PO₄-based photocatalysts developed for dye degradation.

Pollutant	Pollutant conc.	Photocatalyst	Decoration Ag ₃ PO ₄ Method	Ag ₃ PO ₄ Diameter	Dosage (g L ⁻¹)	Irradiation Time (min)	Efficiency (%)	Light Source	[Ref.]
RhB	9 ppm	Ag ₃ PO ₄ /TiO ₂ @Ti ₃ C ₂	In situ precipitation	4–10 nm	0.5	12	97	Solar light	Current study
MO	10 ppm					40	92.4		
MB	10 ppm					6	94		
CV	10 ppm					14	99.2		
RhB	20 µm	Safflower-shaped TiO ₂ /Ti ₃ C ₂	-	-	0.8	60	95	Visible light	[4]
RhB	10 ppm	TiO ₂ @Ti ₃ C ₂ nanoflower	-	-	0.43	40	97	Visible light	[17]
RhB, MO, phenol	0.02 mM, 0.06 mM, 0.2 mM	Ag ₃ PO ₄ /TiO ₂	In situ precipitation	300–500 nm	0.5	15, 80, 90	~100, 90, ~70	Visible light	[19]
RhB	10 ppm	Ag ₃ PO ₄ /TiO ₂ NFs	In situ precipitation	300–360 nm	0.4	10 (Vis)	~100	Visible light	[20]
RhB, MB, pesticides	6 ppm, 8 ppm, -	Ag ₃ PO ₄ /TiO ₂	One pot	100–400 nm	0.5	~6, 4	98, 99.1	Tungsten halogen light	[25]
MB	20 ppm	Ag ₃ PO ₄ /m-TiO ₂	In situ precipitation	~4 nm	0.5	28	100	Visible light	[33]
MB	10 mM	Ag ₃ PO ₄ /TiO ₂ nanosheet film	Impregnating-deposition process	100–300 nm	-	70	98.1	Visible light	[34]
MB	10 ppm	Ag ₃ PO ₄ -TiO ₂ -CNFs	Hydrothermal	20–32 nm	0.5	10	100	Visible light	[35]
MB	10 ppm	Ag ₃ PO ₄ /TiO ₂ NFs	Hydrothermal	-	0.4	15	100	Sunlight	[36]
RhB	10 ppm	CFC/TiO ₂ /Ag ₃ PO ₄	Hydrothermal	20–100 nm	-	100	98.4	Visible light	[37]
MO	20 ppm	Ag ₃ PO ₄ -TiO ₂ -GO	Ion exchange	250–600 nm	1	120	80	Solar light	[38]
RhB	10 ppm	Ag ₃ PO ₄ /TiO ₂	Hydrothermal and ultrasonication	0.1–1.5 µm	1	25	100	Solar light	[31]

**Figure 9.** (a) Effects of scavengers on the RhB photodecomposition. (b) The stability of Ag₃PO₄/TiO₂@Ti₃C₂ (A4) after three consecutive recycling runs.

Along with the photocatalytic efficiency, stability evaluations of photocatalysts are necessary for practical use. Figure 9b shows the RhB degradation efficiency of sample A4 over three consecutive recycling runs. The degradation efficiency was significantly reduced after repeated exposure to solar light, indicating that the photocatalyst was not stable and rapidly deteriorated due to the photocorrosion of Ag₃PO₄ NPs [22]. In the first run, a degradation efficiency of 97% was obtained in 12 min, whereas the degradation efficiencies of RhB were approximately 74% and 39% after the second and third runs, respectively. After a few recycling tests under solar light, the photocorrosion of the catalyst resulted in a low photodecomposition rate by forming an uncontrolled amount of Ag⁰, which can agglomerate and hinder the photocatalytic ability [31].

3.7. Proposed Photocatalytic Mechanism

Based on the obtained scavenger trapping and recycling results, the photocatalytic mechanism of $\text{Ag}_3\text{PO}_4/\text{TiO}_2@\text{Ti}_3\text{C}_2$ is schematically shown in Figure 10. Under solar illumination, electrons from the valence band (VB) of Ag_3PO_4 could be excited to its conduction band (CB), resulting in the formation of holes in the valence band (VB). Since the E_{VB} of TiO_2 is more negative than that of Ag_3PO_4 , holes from Ag_3PO_4 also transferred to TiO_2 and directly degraded RhB, which was absorbed on the surface of TiO_2 during the oxidization process [25,31]. According to literature, the conduction potential of Ag_3PO_4 is higher than the activation energy of single-electron oxygen, preventing photogenerated electrons from being captured by dissolved oxygen.

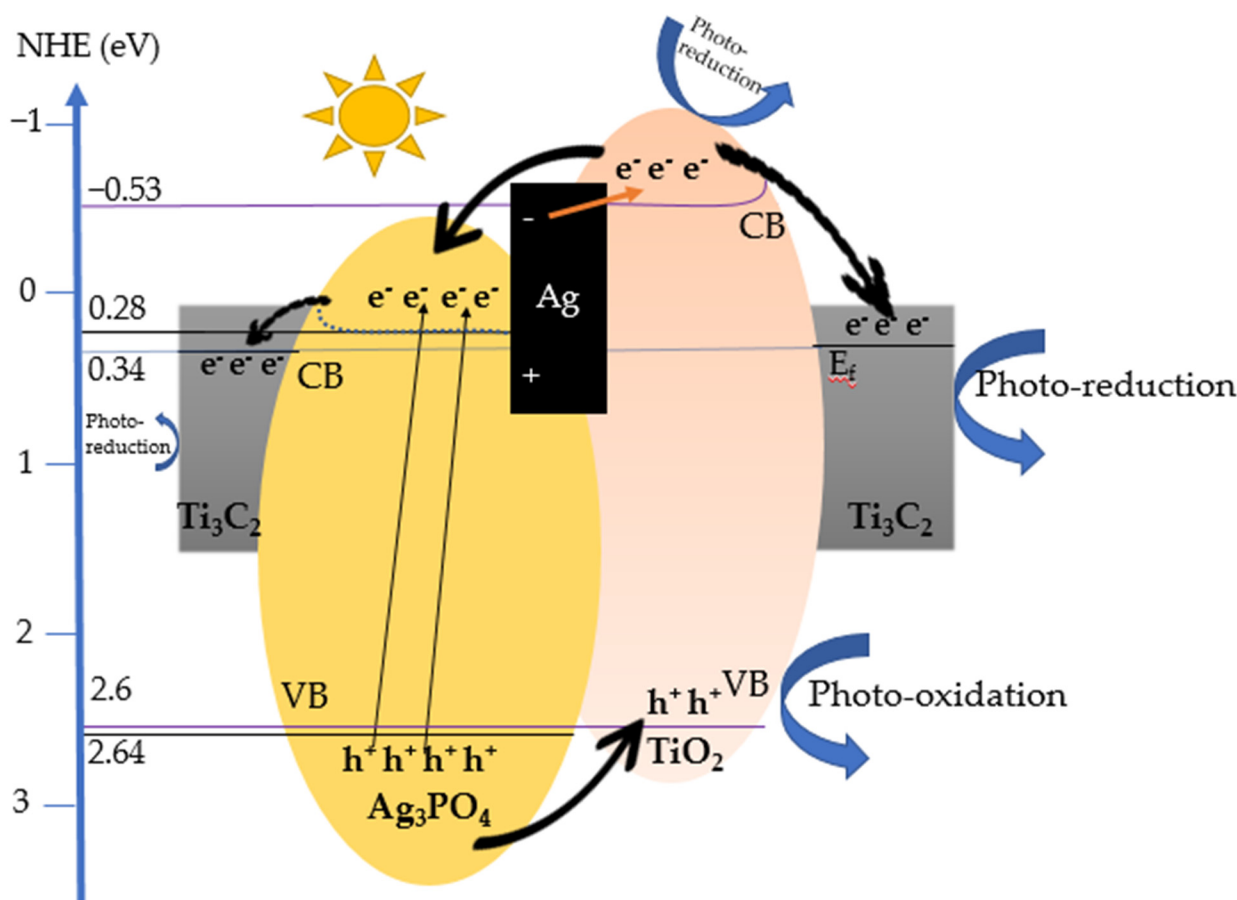
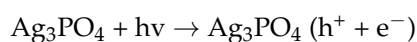
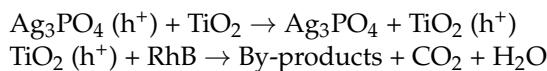


Figure 10. A schematic illustration of the proposed photocatalytic mechanism of $\text{Ag}_3\text{PO}_4/\text{TiO}_2@\text{Ti}_3\text{C}_2$ (A4) exposed to solar light.

Instead, a small amount of Ag is formed as a result of photocorrosion [31]. Electrons and holes in Ag could also be excited by light energy, with electrons migrating to the CB of TiO_2 , while the remaining holes could be recombined with photoexcited electrons in Ag_3PO_4 CB, thereby, partially preventing further corrosion [31]. Furthermore, some electrons were transferred from TiO_2 and Ag_3PO_4 to Ti_3C_2 MXene, resulting in band bending and the formation of a Schottky junction as well as a uniform Fermi level [4,17,39]. The photo-reduction reaction occurring on the surface of Ti_3C_2 and the TiO_2 conduction band generated $\bullet\text{O}_2^-$ radicals, which are required for effective RhB decomposition. The production of $\bullet\text{O}_2^-$ and h^+ could easily degrade a variety of dyes, including RhB, MB, CV, and MO, under solar light. The proposed mechanism is consistent with scavenger trapping experiments and is formulated as follows:

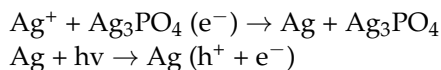
1. **Photo-oxidation reaction:**



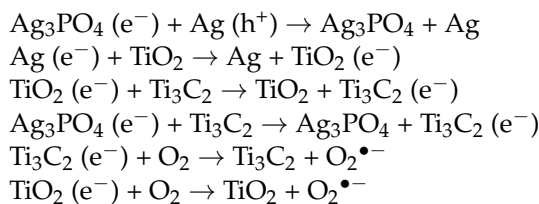


2. Photo-reduction reaction:

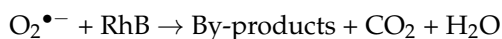
- Photoexcited electrons and separation of e^-/h^+ :



- Transfer routes and formation of $\text{O}_2^{\bullet-}$:



- Degradation of pollutants:



Based on this proposed mechanism, the stability of the composite did not significantly improve. This might be due to a longer electron transfer distance between TiO_2 and Ti_3C_2 than between Ag_3PO_4 and Ti_3C_2 . Second, an unknown amount of Ti_3C_2 on the surface and/or insufficient interfacial contact between Ag_3PO_4 and Ti_3C_2 might lower the composite's stability. Both reasons could not prevent the rapid formation of Ag, reducing the stability and photocatalytic performance of the composite.

4. Conclusions

This study successfully synthesized $\text{Ag}_3\text{PO}_4/\text{TiO}_2@\text{Ti}_3\text{C}_2$ composites by precipitating Ag_3PO_4 NPs on the surface of $\text{TiO}_2@\text{Ti}_3\text{C}_2$ flowers. Some characterization methods were conducted to investigate the surface morphology, structural composition, surface area, and optical properties of $\text{Ag}_3\text{PO}_4/\text{TiO}_2@\text{Ti}_3\text{C}_2$. The characteristics of Ag_3PO_4 -deposited $\text{TiO}_2@\text{Ti}_3\text{C}_2$ endow superior photocatalytic activities in the comparison with $\text{TiO}_2@\text{Ti}_3\text{C}_2$, pristine Ag_3PO_4 , and $\text{Ag}_3\text{PO}_4/\text{TiO}_2$ P25, particularly sample A4. This composite exhibited excellent photocatalytic performance for various organic dyes (degraded 97% RhB, 94% MB, 99% CV, and 92% MO) within a short period of time when exposed to solar light irradiation.

The high photocatalytic activity of the composite was due to the high surface area of $\text{TiO}_2@\text{Ti}_3\text{C}_2$ with small Ag_3PO_4 particles (4–10 nm) that can easily reach dye molecules. The e^-/h^+ transfer throughout the composite system also contributes to increased charging transfer, expanded light absorption wavelength, and decreased electron–hole pair recombination, which gives synergistic effects for photocatalytic activity. Based on the scavenger trapping and recycling test results, the mechanism was proposed.

Supplementary Materials: The following are available online at <https://www.mdpi.com/article/10.3390/nano12142464/s1>, Figure S1: EDS patterns of $\text{Ag}_3\text{PO}_4/\text{TiO}_2@\text{Ti}_3\text{C}_2$ (sample A4); the inset image shows an SEM image of the sample, Figure S2: SAED image of $\text{Ag}_3\text{PO}_4/\text{TiO}_2@\text{Ti}_3\text{C}_2$ (sample A4) taken of an arbitrary area, Figure S3: XPS survey spectra of Ti_3C_2 , $\text{TiO}_2@\text{Ti}_3\text{C}_2$, and $\text{Ag}_3\text{PO}_4/\text{TiO}_2@\text{Ti}_3\text{C}_2$, Figure S4: (a) F 1s high-resolution XPS spectra of Ti_3C_2 , and (b–c) Ag 3d and P 1s high-resolution XPS spectra of $\text{Ag}_3\text{PO}_4/\text{TiO}_2@\text{Ti}_3\text{C}_2$ (sample A4), Figure S5: Photodegradation absorption spectra of (a) Methylene Blue, (b) Crystal Violet, and (c) Methylene Orange under solar light.

Author Contributions: Conceptualization, N.T.A.N.; methodology, N.T.A.N.; software, N.T.A.N.; validation, N.T.A.N. and H.K.; formal analysis, N.T.A.N.; investigation, N.T.A.N.; resources, N.T.A.N. and H.K.; data curation, N.T.A.N. and H.K.; writing—original draft preparation, N.T.A.N.; writing—review and editing, N.T.A.N. and H.K.; visualization, N.T.A.N.; supervision, H.K.; project adminis-

tration, H.K.; funding acquisition, H.K. All authors have read and agreed to the published version of the manuscript.

Funding: This research was funded in part by the Korea Institute of Energy Technology Evaluation and Planning (KETEP) and the Ministry of Trade, Industry & Energy (MOTIE) of the Republic of Korea (No. 20203010040010) and in part by the Korea Evaluation Institute of Industrial Technology (KEIT) and the Ministry of Trade, Industry & Energy (MOTIE) of the Republic of Korea (No. 200153646).

Institutional Review Board Statement: Not applicable.

Informed Consent Statement: Not applicable.

Data Availability Statement: The data presented in this study are available on request from the corresponding author.

Acknowledgments: The authors deeply appreciate Professor Sang-Wha Lee at Gachon University for his valuable advice on this study.

Conflicts of Interest: The authors declare no conflict of interest. The funders had no role in the design of the study; in the collection, analyses, or interpretation of data; in the writing of the manuscript, or in the decision to publish the results.

References

1. Li, P.; Karunanidhi, D.; Subramani, T.; Srinivasamoorthy, K. Sources and Consequences of Groundwater Contamination. *Arch. Environ. Contam. Toxicol.* **2021**, *80*, 1–10. [[CrossRef](#)] [[PubMed](#)]
2. Schweitzer, L.; Noblet, J. Water Contamination and Pollution. In *Green Chemistry—An Inclusive Approach*; Elsevier: Amsterdam, The Netherlands, 2018; pp. 261–290. [[CrossRef](#)]
3. My Tran, N.; Thanh Hoai Ta, Q.; Sreedhar, A.; Noh, J.S. Ti₃C₂T_x MXene playing as a strong methylene blue adsorbent in wastewater. *Appl. Surf. Sci.* **2021**, *537*, 148006. [[CrossRef](#)]
4. My Tran, N.; Thanh Hoai Ta, Q.; Noh, J.S. Unusual synthesis of safflower-shaped TiO₂/Ti₃C₂ heterostructures initiated from two-dimensional Ti₃C₂ MXene. *Appl. Surf. Sci.* **2021**, *538*, 148023. [[CrossRef](#)]
5. Muneer, I.; Farrukh, M.A.; Ali, D.; Bashir, F. Heterogeneous photocatalytic degradation of organic dyes by highly efficient GdCoSnO₃. *Mater. Sci. Eng. B Solid-State Mater. Adv. Technol.* **2021**, *265*, 115028. [[CrossRef](#)]
6. Ton, N.N.T.; Dao, A.T.N.; Kato, K.; Ikenaga, T.; Trinh, D.X.; Taniike, T. One-pot synthesis of TiO₂/graphene nanocomposites for excellent visible light photocatalysis based on chemical exfoliation method. *Carbon* **2018**, *133*, 109–117. [[CrossRef](#)]
7. Kadam, R.L.; Kim, Y.; Gaikwad, S.; Chang, M.; Tarte, N.H.; Han, S. Catalytic decolorization of rhodamine B, Congo red, and crystal violet dyes, with a novel niobium oxide anchored molybdenum (Nb–O–Mo). *Catalysts* **2020**, *10*, 491. [[CrossRef](#)]
8. Chiu, Y.H.; Chang, T.F.M.; Chen, C.Y.; Sone, M.; Hsu, Y.J. Mechanistic insights into photodegradation of organic dyes using heterostructure photocatalysts. *Catalysts* **2019**, *9*, 430. [[CrossRef](#)]
9. Ghaffar, A.; Zhang, L.; Zhu, X.; Chen, B. Porous PVdF/GO Nanofibrous Membranes for Selective Separation and Recycling of Charged Organic Dyes from Water. *Environ. Sci. Technol.* **2018**, *52*, 4265–4274. [[CrossRef](#)]
10. Pal, B.; Kaur, R.; Grover, I.S. Superior adsorption and photodegradation of eriochrome black-T dye by Fe³⁺ and Pt⁴⁺ impregnated TiO₂ nanostructures of different shapes. *J. Ind. Eng. Chem.* **2016**, *33*, 178–184. [[CrossRef](#)]
11. Sacco, O.; Vaiano, V.; Rizzo, L.; Sannino, D. Photocatalytic activity of a visible light active structured photocatalyst developed for municipal wastewater treatment. *J. Clean. Prod.* **2018**, *175*, 38–49. [[CrossRef](#)]
12. Etacheri, V.; Di Valentin, C.; Schneider, J.; Bahnemann, D.; Pillai, S.C. Visible-light activation of TiO₂ photocatalysts: Advances in theory and experiments. *J. Photochem. Photobiol. C Photochem. Rev.* **2015**, *25*, 1–29. [[CrossRef](#)]
13. Daghrir, R.; Drogui, P.; Robert, D. Modified TiO₂ for environmental photocatalytic applications: A review. *Ind. Eng. Chem. Res.* **2013**, *52*, 3581–3599. [[CrossRef](#)]
14. Wang, Y.; He, Y.; Lai, Q.; Fan, M. Review of the progress in preparing nano TiO₂: An important environmental engineering material. *J. Environ. Sci.* **2014**, *26*, 2139–2177. [[CrossRef](#)] [[PubMed](#)]
15. Ansari, S.A.; Cho, M.H. Highly Visible Light Responsive, Narrow Band gap TiO₂ Nanoparticles Modified by Elemental Red Phosphorus for Photocatalysis and Photoelectrochemical Applications. *Sci. Rep.* **2016**, *6*, 25405. [[CrossRef](#)]
16. Li, Y.; Deng, X.; Tian, J.; Liang, Z.; Cui, H. Ti₃C₂ MXene-derived Ti₃C₂/TiO₂ nanoflowers for noble-metal-free photocatalytic overall water splitting. *Appl. Mater. Today* **2018**, *13*, 217–227. [[CrossRef](#)]
17. Quyen, V.T.; Ha, L.T.T.; Thanh, D.M.; van Le, Q.; Viet, N.M.; Nham, N.T.; Thang, P.Q. Advanced synthesis of MXene-derived nanoflower-shaped TiO₂@Ti₃C₂ heterojunction to enhance photocatalytic degradation of Rhodamine B. *Environ. Technol. Innov.* **2021**, *21*, 101286. [[CrossRef](#)]
18. Frontistis, Z.; Antonopoulou, M.; Petala, A.; Venieri, D.; Konstantinou, I.; Kondarides, D.I.; Mantzavinos, D. Photodegradation of ethyl paraben using simulated solar radiation and Ag₃PO₄ photocatalyst. *J. Hazard. Mater.* **2017**, *323*, 478–488. [[CrossRef](#)]

19. Zhao, F.M.; Pan, L.; Wang, S.; Deng, Q.; Zou, J.J.; Wang, L.; Zhang, X. Ag₃PO₄/TiO₂ composite for efficient photodegradation of organic pollutants under visible light. *Appl. Surf. Sci.* **2014**, *317*, 833–838. [[CrossRef](#)]
20. Xie, J.; Yang, Y.; He, H.; Cheng, D.; Mao, M.; Jiang, Q.; Song, L.; Xiong, J. Facile synthesis of hierarchical Ag₃PO₄/TiO₂ nanofiber heterostructures with highly enhanced visible light photocatalytic properties. *Appl. Surf. Sci.* **2015**, *355*, 921–929. [[CrossRef](#)]
21. Khalid, N.R.; Mazia, U.; Tahir, M.B.; Niaz, N.A.; Javid, M.A. Photocatalytic degradation of RhB from an aqueous solution using Ag₃PO₄/N-TiO₂ heterostructure. *J. Mol. Liq.* **2020**, *313*, 113522. [[CrossRef](#)]
22. Ma, X.; Li, H.; Wang, Y.; Li, H.; Liu, B.; Yin, S.; Sato, T. Substantial change in phenomenon of “self-corrosion” on Ag₃PO₄/TiO₂ compound photocatalyst. *Appl. Catal. B Environ.* **2014**, *158–159*, 314–320. [[CrossRef](#)]
23. Chen, X.; Dai, Y.; Wang, X. Methods and mechanism for improvement of photocatalytic activity and stability of Ag₃PO₄: A review. *J. Alloys Compd.* **2015**, *649*, 910–932. [[CrossRef](#)]
24. Nekouei, F.; Nekouei, S.; Pouzesh, M.; Liu, Y. Porous-CdS/Cu₂O/graphitic-C₃N₄ dual p-n junctions as highly efficient photo/catalysts for degrading ciprofloxacin and generating hydrogen using solar energy. *Chem. Eng. J.* **2020**, *385*, 123710. [[CrossRef](#)]
25. Nyankson, E.; Efavi, J.K.; Agyei-Tuffour, B.; Manu, G. Synthesis of TiO₂-Ag₃PO₄ photocatalyst material with high adsorption capacity and photocatalytic activity: Application in the removal of dyes and pesticides. *RSC Adv.* **2021**, *11*, 17032–17045. [[CrossRef](#)]
26. Zanella, R.; Giorgio, S.; Henry, C.R.; Louis, C. Alternative methods for the preparation of gold nanoparticles supported on TiO₂. *J. Phys. Chem. B* **2002**, *106*, 7634–7642. [[CrossRef](#)]
27. Kong, F.; He, X.; Liu, Q.; Qi, X.; Zheng, Y.; Wang, R.; Bai, Y. Improving the electrochemical properties of MXene Ti₃C₂ multilayer for Li-ion batteries by vacuum calcination. *Electrochim. Acta* **2018**, *265*, 140–150. [[CrossRef](#)]
28. Cao, M.; Wang, F.; Wang, L.; Wu, W.; Lv, W.; Zhu, J. Room Temperature Oxidation of Ti₃C₂ MXene for Supercapacitor Electrodes. *J. Electrochem. Soc.* **2017**, *164*, A3933–A3942. [[CrossRef](#)]
29. Shen, C.; Wang, L.; Zhou, A.; Wang, B.; Wang, X.; Lian, W.; Hu, Q.; Qin, G.; Liu, X. Synthesis and electrochemical properties of two-dimensional RGO/Ti₃C₂T_x nanocomposites. *Nanomaterials* **2018**, *8*, 80. [[CrossRef](#)]
30. Xia, Q.X.; Fu, J.; Yun, J.M.; Mane, R.S.; Kim, K.H. High volumetric energy density annealed-MXene-nickel oxide/MXene asymmetric supercapacitor. *RSC Adv.* **2017**, *7*, 11000–11011. [[CrossRef](#)]
31. Liu, W.; Liu, D.; Wang, K.; Yang, X.; Hu, S.; Hu, L. Fabrication of Z-scheme Ag₃PO₄/TiO₂ Heterostructures for Enhancing Visible Photocatalytic Activity. *Nanoscale Res. Lett.* **2019**, *14*, 203. [[CrossRef](#)]
32. Azeez, F.; Al-Hetlani, E.; Arafa, M.; Abdelmonem, Y.; Nazeer, A.A.; Amin, M.O.; Madkour, M. The effect of surface charge on photocatalytic degradation of methylene blue dye using chargeable titania nanoparticles. *Sci. Rep.* **2018**, *8*, 7104. [[CrossRef](#)] [[PubMed](#)]
33. Li, Y.; Yu, L.; Li, N.; Yan, W.; Li, X. Heterostructures of Ag₃PO₄/TiO₂ mesoporous spheres with highly efficient visible light photocatalytic activity. *J. Colloid Interface Sci.* **2015**, *450*, 246–253. [[CrossRef](#)] [[PubMed](#)]
34. Tang, C.; Liu, E.; Fan, J.; Hu, X.; Kang, L.; Wan, J. Heterostructured Ag₃PO₄/TiO₂ nano-sheet film with high efficiency for photodegradation of methylene blue. *Ceram. Int.* **2014**, *40*, 15447–15453. [[CrossRef](#)]
35. Pant, B.; Prasad Ojha, G.; Acharya, J.; Park, M. Ag₃PO₄-TiO₂-Carbon nanofiber Composite: An efficient Visible-light photocatalyst obtained from electrospinning and hydrothermal methods. *Sep. Purif. Technol.* **2021**, *276*, 119400. [[CrossRef](#)]
36. Saud, P.S.; Pant, B.; Twari, A.P.; Ghouri, Z.K.; Park, M.; Kim, H.Y. Effective photocatalytic efficacy of hydrothermally synthesized silver phosphate decorated titanium dioxide nanocomposite fibers. *J. Colloid Interface Sci.* **2016**, *465*, 225–232. [[CrossRef](#)]
37. Zhang, Y.; Duoerkun, G.; Shi, Z.; Cao, W.; Liu, T.; Liu, J.; Zhang, L.; Li, M.; Chen, Z. Construction of TiO₂/Ag₃PO₄ nanojunctions on carbon fiber cloth for photocatalytically removing various organic pollutants in static or flowing wastewater. *J. Colloid Interface Sci.* **2020**, *571*, 213–221. [[CrossRef](#)]
38. Sheu, F.J.; Cho, C.P.; Liao, Y.T.; Yu, C.T. Ag₃PO₄-TiO₂-graphene oxide ternary composites with efficient photodegradation, hydrogen evolution, and antibacterial properties. *Catalysts* **2018**, *8*, 57. [[CrossRef](#)]
39. Cai, T.; Wang, L.; Liu, Y.; Zhang, S.; Dong, W.; Chen, H.; Yi, X.; Yuan, J.; Xia, X.; Liu, C.; et al. Ag₃PO₄/Ti₃C₂ MXene interface materials as a Schottky catalyst with enhanced photocatalytic activities and anti-photocorrosion performance. *Appl. Catal. B Environ.* **2018**, *239*, 545–554. [[CrossRef](#)]